NANO LETTERS

pubs.acs.org/NanoLett Letter

Turning Nonemissive $CsPb_2Br_5$ Crystals into High-Performance Scintillators through Alkali Metal Doping

Jian Qiu, He Zhao, Zhen Mu, Jiaye Chen, Hao Gu, Chang Gu, Guichuan Xing,* Xian Qin,* and Xiaogang Liu*

Cite This: https://doi.org/10.1021/acs.nanolett.3c04455 Read Online

ACCESS | Metrics & More | Article Recommendations | Supporting Information

ABSTRACT: X-ray scintillators have utility in radiation detection, therapy, and imaging. Various materials, such as halide perovskites, organic illuminators, and metal clusters, have been developed to replace conventional scintillators due to their ease of fabrication, improved performance, and adaptability. However, they suffer from self-absorption, chemical instability, and weak X-ray stopping power. Addressing these limitations, we employ alkali metal doping to turn nonemissive $CsPb_2Br_5$ into scintillators. Introducing alkali metal dopants causes lattice distortion and enhances electron−phonon coupling, which creates transient potential energy wells capable of trapping photogenerated or X-ray-generated electrons and holes to form self-trapped excitons. These self-trapped excitons undergo radiative recombination, resulting in a photoluminescence quantum yield of 55.92%. The $CsPb_2Br_5$-based X-ray scintillator offers strong X-ray stopping power, high resistance to self-absorption, and enhanced stability when exposed to the atmosphere, chemical solvents, and intense irradiation. It exhibits a detection limit of 162.3 nGy_{air} s^{-1} and an imaging resolution of 21 lp mm^{-1}.

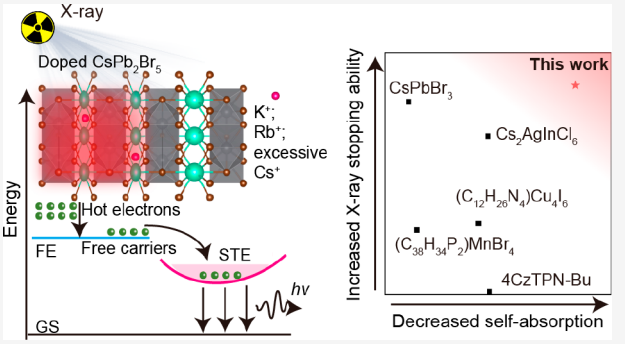

KEYWORDS: *perovskites, ion doping, self-trapped exciton states, scintillators, X-ray imaging*

Scintillators, which convert high-energy radiation into low-energy photons, have widespread applications in fields ranging from radiation detection and photodynamic therapy to medical imaging.[1−10] Traditional materials, such as bulk-formed $CdWO_4$, activator-doped NaI:TI, and organic BC-408, have been commercially used as X-ray scintillators. However, they suffer from limitations such as challenging fabrication conditions, limited optical tunability, and low light yields in plastic scintillators.[11−13] To overcome these limitations, halide perovskites,[14−17] organic luminescent molecules,[18−20] and metal clusters[21−23] have been developed. These materials offer a high photoluminescence efficiency, high-throughput solution fabrication, and improved flexibility. However, halide perovskites suffer from severe self-absorption due to their inherent bandgap emission, limiting their scintillation performance.[24] Moreover, their ionic structure makes them highly susceptible to moisture-induced instability.[25,26] On the other hand, scintillators based on organic luminescent molecules or metal clusters show reduced self-absorption but lack sufficient X-ray stopping ability.[27,28] Therefore, the quest for stable scintillator materials that simultaneously address self-absorption issues and offer strong X-ray stopping power remains crucial for advancing the scintillation performance.

$CsPb_2Br_5$, analogous to the well-known $CsPbBr_3$ scintillator, holds promise for a strong X-ray stopping capability. Moreover, $CsPb_2Br_5$ features an absorption edge beyond the visible emission range, eliminating self-absorption during visible irradiation, making it ideal for nonlinear optics and lasers.[29] Its low-dimensional layered crystal structure enhances chemical and environmental stability.[30,31] Hence, $CsPb_2Br_5$ offers potential as a stable X-ray scintillator with both non-self-absorption and robust X-ray stopping power. However, pristine $CsPb_2Br_5$, with its perfect crystal lattice, has an indirect bandgap and thus no bandgap emission.[29] To the best of our knowledge, no reports existed on the utilization of single-crystalline $CsPb_2Br_5$ as an X-ray scintillator. In this work, we report a doping method to activate the "dark" $CsPb_2Br_5$ into a high-performance X-ray scintillator (Figure 1). The emission at ∼700 nm in $CsPb_2Br_5$ arises from self-trapped excitons (STEs) localized in the potential wells. The corresponding excitonic states become radiative due to pronounced electron−phonon coupling resulting from lattice distortion caused by the

Received: November 16, 2023
Revised: January 12, 2024
Accepted: January 18, 2024

https://doi.org/10.1021/acs.nanolett.3c04455
Nano Lett. XXXX, XXX, XXX−XXX

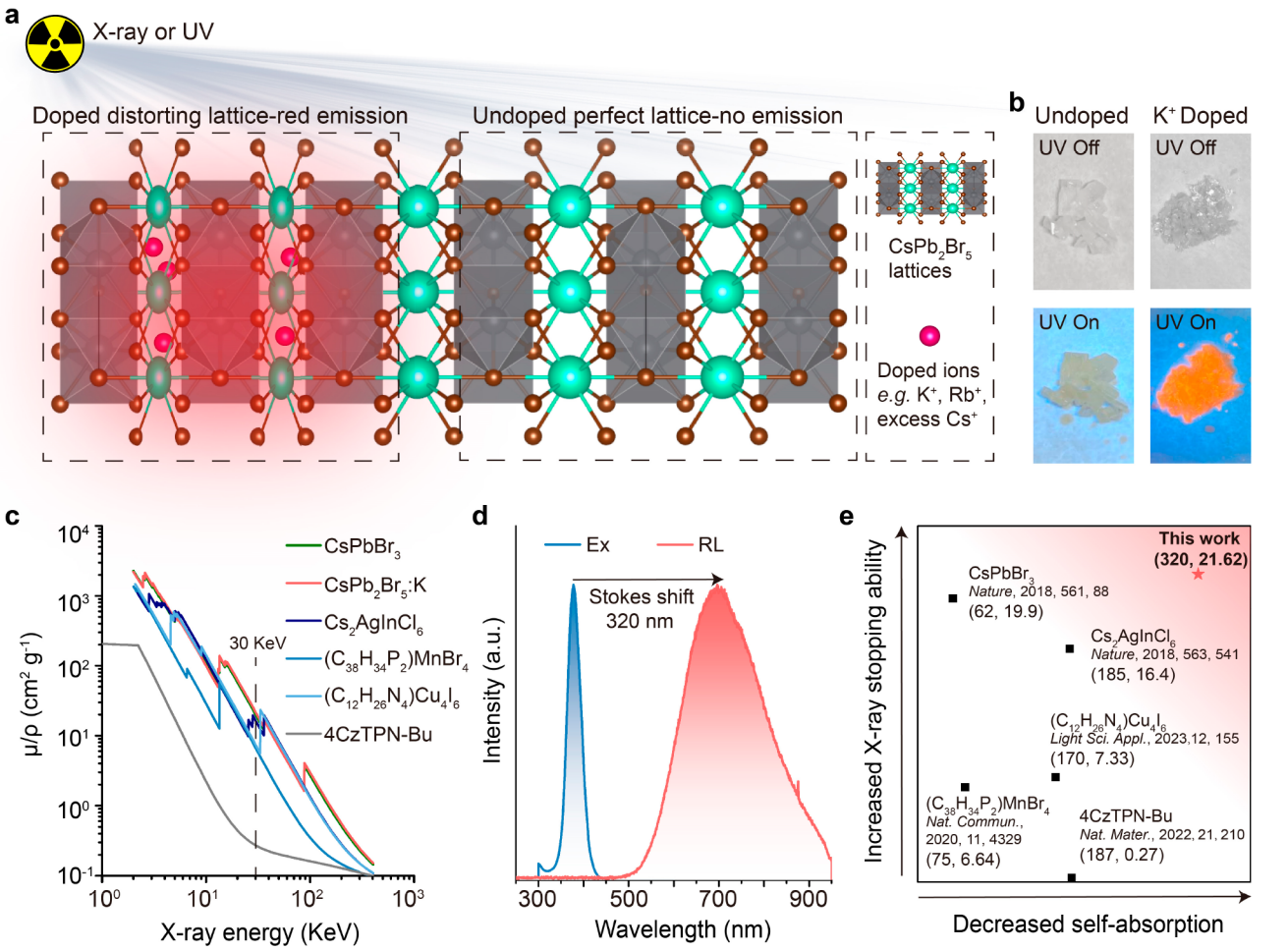

Figure 1. Doping-induced radioluminescence in $CsPb_2Br_5$ through lattice distortion. **a**, Schematic of emission in alkali-metal-doped $CsPb_2Br_5$ from self-trapped exciton states induced by lattice distortion. **b**, Visual comparison of undoped $CsPb_2Br_5$ and K^+-doped $CsPb_2Br_5$ under both daylight and UV excitation. **c**, Mass attenuation coefficients of various scintillation materials plotted as a function of X-ray energy. **d**, Excitation spectrum and radioluminescence (RL) of K^+-doped $CsPb_2Br_5$. **e**, Comparative analysis of X-ray stopping ability and self-absorption among current X-ray scintillators (Stokes shift in nm and mass attenuation coefficient at an X-ray energy of 30 keV/cm^2 g^{-1}).

introduction of alkali metal ions such as K^+, Rb^+, or an excess of Cs^+ (Figure 1a).

Both undoped and doped $CsPb_2Br_5$ crystals were synthesized in an aqueous solution by using a modified solvent evaporation method. The undoped $CsPb_2Br_5$ appears as a transparent crystal but lacks intrinsic bandgap emission (Figure 1b). $CsPb_2Br_5$ has a layered crystal structure with a soft lattice, making it suitable for producing lattice-distortion-induced emission, including luminescence from permanent defects or STE.[32−35] Based on this theory, alkali metal cations, such as K^+, Rb^+, or an excess of Cs^+, were introduced as dopants into $CsPb_2Br_5$, facilitating transient or permanent lattice distortion and subsequently inducing emission. Notably, all attempted cationic dopants (K^+, Rb^+, and excessive Cs^+) were found to induce a red emission with a broad peak in $CsPb_2Br_5$ (Figure 1b and Supplementary Figure 1).

For instance, considering K^+-doped $CsPb_2Br_5$ ($CsPb_2Br_5$:K), this material shows a similarly strong X-ray mass attenuation coefficient as $CsPbBr_3$ (Figure 1c). It surpasses other reported scintillators across a wide X-ray energy range, spanning from 1 to 400 keV. These materials include double halide perovskite $Cs_2AgInCl_6$, metal clusters $(C_{38}H_{34}P_2)MnBr_4$ and $(C_{12}H_{26}N_4)$-Cu_4I_6, and the organic thermally activated delayed fluorescence (TADF) molecule 4CzTPN-Bu.[19,21,33,36] Furthermore, the X-ray-excited radioluminescence (RL) of $CsPb_2Br_5$:K exhibits a large Stokes shift of ∼320 nm (Figure 1d). This pronounced shift largely alleviates self-absorption in X-ray scintillators. Compared with other scintillation materials, the $CsPb_2Br_5$:K material in this work shows a clear advantage in terms of concurrently achieving reduced self-absorption and strong X-ray stopping ability (Figure 1e).

To further investigate the effect of cation doping on the crystal structure of $CsPb_2Br_5$, we performed X-ray diffraction (XRD) analysis for samples with and without K^+ (Figure 2a). Both samples exhibited identical diffraction peaks, corresponding to the tetragonal crystal structure of the $CsPb_2Br_5$ host (PDF#25-0211). This suggests that K^+ doping barely alters the host crystal structure, as evident by the presence of identical sharp and discrete Bragg diffraction spots in the electron diffraction patterns for both samples (Figure 2b). However, a noticeable shift of the peaks corresponding to (002) and (112) planes toward larger diffraction angles (2θ) is evident in the sample with K^+ doping (Figure 2a and Supplementary Figure 2). According to the diffraction equation

$$2d \sin\theta = n\lambda \quad (1)$$

where d is the interplanar spacing, θ is the diffraction angle in degrees, n is the integer coefficient in front of the wavelength λ,

https://doi.org/10.1021/acs.nanolett.3c04455
Nano Lett. XXXX, XXX, XXX−XXX

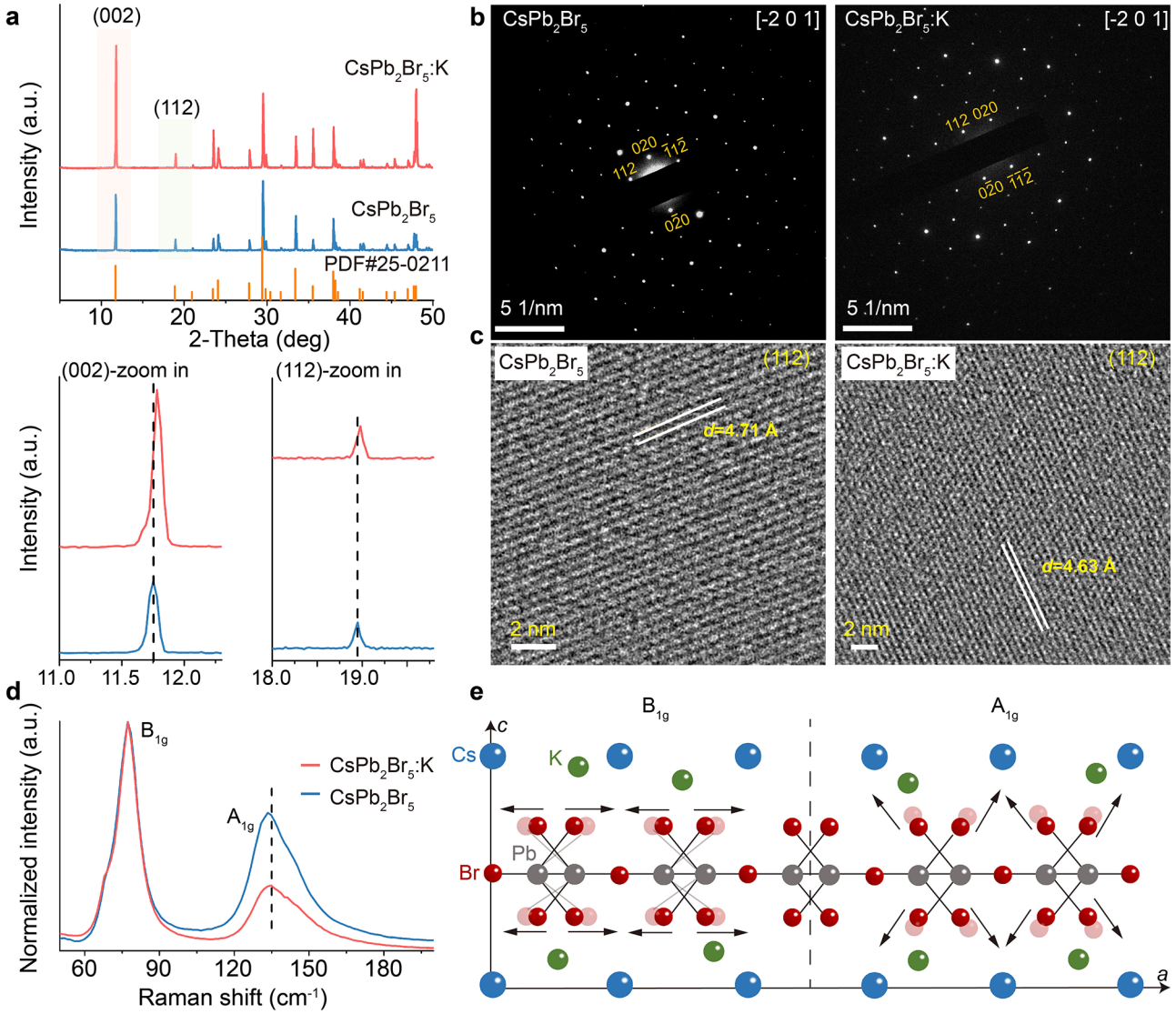

Figure 2. K^+-doping-induced lattice contraction in $CsPb_2Br_5$. **a**, XRD patterns of $CsPb_2Br_5$ with and without K^+ doping. The XRD peaks corresponding to the (002) and (112) planes exhibit a shift toward larger 2θ upon K^+ doping. **b**, Electron diffraction patterns for $CsPb_2Br_5$ with and without K^+ doping. **c**, High-resolution TEM images of (112) planes in $CsPb_2Br_5$ with and without K^+ doping. **d**, Raman spectra of $CsPb_2Br_5$ with and without K^+ doping. **e**, Schematic of atomic displacements corresponding to the non-degenerate Raman mode in $CsPb_2Br_5$ with K^+ doping.

and $n\lambda$ is a constant. From eq 1, it is apparent that a smaller interplanar spacing d leads to a large diffraction angle θ. Thus, the shift of 2θ to larger values reveals that K^+ cations, being smaller in atomic size compared to Cs^+, induce a slight crystal contraction of the $CsPb_2Br_5$ lattice upon doping.

High-resolution transmission electron microscopy (TEM) images of (112) planes for samples with and without K^+ dopants confirm a reduction in interplanar spacing from ~4.71 Å in the undoped sample to ~4.63 Å in the K^+-doped sample (Figure 2c). To ascertain the doping site, we investigated the Pb−Br phonon modes, which are highly influenced by ion doping, using Raman spectroscopy (Figure 2d). Compared with the undoped sample, K^+-doped $CsPb_2Br_5$ exhibited a blue shift in the Raman mode A_{1g}, while the position of Raman mode B_{1g} remains unchanged. Raman mode B_{1g} refers to the atomic displacement of Br along the a axis, implying that cation doping has a negligible effect on the lattice parameter along the a axis.[37] The vertically resolved component of Raman mode A_{1g} represents the atomic displacement of Br along the c axis,[37] and the blue shift indicates that K^+ dopants enhance the Pb−Br vibration along the c axis. This suggests that K^+ dopants mainly substitute Cs^+ located between two Pb−Br layers, inducing lattice contraction due to their smaller size compared to Cs^+ (Figure 2e). This observation is in line with the results obtained from XRD and high-resolution TEM.

To understand the luminescence mechanism in doped $CsPb_2Br_5$, we first employed DFT calculations to investigate the electronic properties of $CsPb_2Br_5$ and K^+-doped $CsPb_2Br_5$. Our goal was to assess how the incorporation of K^+ dopants affects the band structure. It is worth noting that the K^+ concentration in the doped $CsPb_2Br_5$ is exceedingly low, at approximately 0.5% (Supplementary Figure 3 and Supplementary Tables 1 and 2). Consequently, we used a computational model that reflects this minimal K^+ substitution (Supplementary Figure 4). The computational results demonstrated that K^+ dopants have negligible effects on the band structure and density of states, supporting our expectation that the luminescence observed in $CsPb_2Br_5$:K primarily results

https://doi.org/10.1021/acs.nanolett.3c04455
Nano Lett. XXXX, XXX, XXX−XXX

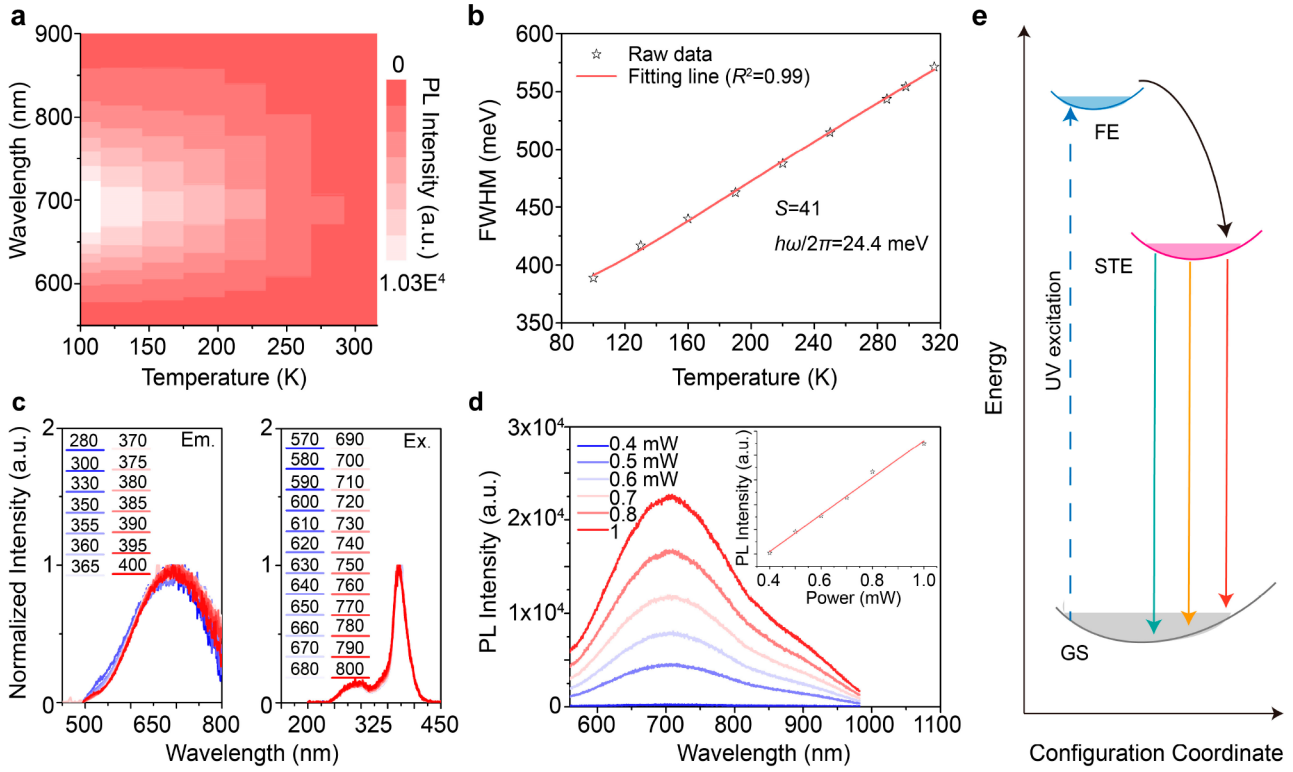

Figure 3. Mechanistic investigation of red emission from self-trapped exciton (STE) states in $CsPb_2Br_5$:K. a, Photoluminescence spectra of $CsPb_2Br_5$:K at various temperatures. **b**, Results of full width at half-maximum as a function of temperature. **c**, Left: emission spectrum of $CsPb_2Br_5$:K under different excitation wavelengths. Right: excitation spectrum of $CsPb_2Br_5$:K corresponding to varying emission wavelengths. **d**, Emission spectrum of $CsPb_2Br_5$:K under excitation with different power densities. Inset: fitting results of the emission intensity as a function of excitation power. **e**, Schematic illustrating the emission mechanism involving STE in $CsPb_2Br_5$:K.

from lattice distortion rather than band edges. To further distinguish whether the luminescence originates from permanent lattice defects or STE, we performed temperature-dependent photoluminescence spectroscopy (Figure 3a and b). The Huang–Rhys factor (S), which indicates the strength of electron–phonon coupling, was calculated using eq 2[33]

$$\mathrm{FWHM} = 2.36\sqrt{S}\,\frac{h}{2\pi}\omega_{\mathrm{phonon}}\sqrt{\cot\frac{\frac{h}{2\pi}\omega_{\mathrm{phonon}}}{2k_{\mathrm{B}}T}} \qquad (2)$$

where $h/2\pi^*\omega_{\mathrm{phonon}}$ denotes the phonon frequency, k_{B} is Boltzmann's constant, and T is the temperature. The calculated S value was 41 with a phonon frequency of 24.4 meV. This high S indicates strong electron–phonon coupling, suggesting a dopant-softened lattice. In this regard, transient lattice distortion within the nanoscale domain is likely to form in $CsPb_2Br_5$:K upon photoexcitation, resulting in trapped excitons.

Normalized emission spectra under different excitation wavelengths and normalized excitation spectra corresponding to different emission wavelengths were examined (Figure 3c). It was observed that all emission and excitation spectra exhibited identical shapes and features, indicating that the red emission arises from the relaxation of the same excited states.[38] Moreover, the intensity of emission in $CsPb_2Br_5$:K exhibited a linear relationship with excitation power without reaching saturation (Figure 3d). The possibility of emission from phase impurities like KPb_2Br_5, which may form in K^+-doped $CsPb_2Br_5$, was ruled out (Supplementary Figure 5). These results support the conclusion that the luminescence in $CsPb_2Br_5$:K, characterized by notable features such as a broad red emission, a long carrier lifetime of ~45 μs, and a high photoluminescence quantum yield (PLQY) of 55.92%, is primarily a result of STEs (Figure 3e and Supplementary Figures 6 and 7). These STEs are mainly a result of strong electron–phonon coupling induced by dopants, causing photoexcited transient lattice distortion within dopant-centered nanodomains rather than originating from permanent lattice defects or impurities. Furthermore, the addition of increased quantities of K^+ to $CsPb_2Br_5$ crystals, without disrupting their tetragonal structure, results in a more significant contraction of the crystal lattice. This contraction intensifies the electron–phonon coupling, thus improving the STE (Supplementary Figure 7a and Supporting Information Table 2). Similarly, other ion dopants (Rb^+ and excess Cs^+) in $CsPb_2Br_5$ also induced photoexcited transient slight lattice distortions, leading to red emission attributed to STE states (Supplementary Figures 8–12).

The mechanism of radioluminescence in $CsPb_2Br_5$:K scintillators appears highly likely to be the same as that of photoluminescence, which arises from STEs, due to the overlapping spectra of the two processes (Figure 4a). When X-rays interact with the inner-shell electrons of heavy atoms in $CsPb_2Br_5$:K, they trigger the photoelectric effect and Compton scattering, generating secondary X-rays. These then excite $CsPb_2Br_5$:K and subsequently produce high-energy hot electrons and holes, which become free carriers upon thermalization and eventually form free excitons. Finally, these free excitons diffuse to the potential wells or regions of

https://doi.org/10.1021/acs.nanolett.3c04455
Nano Lett. XXXX, XXX, XXX−XXX

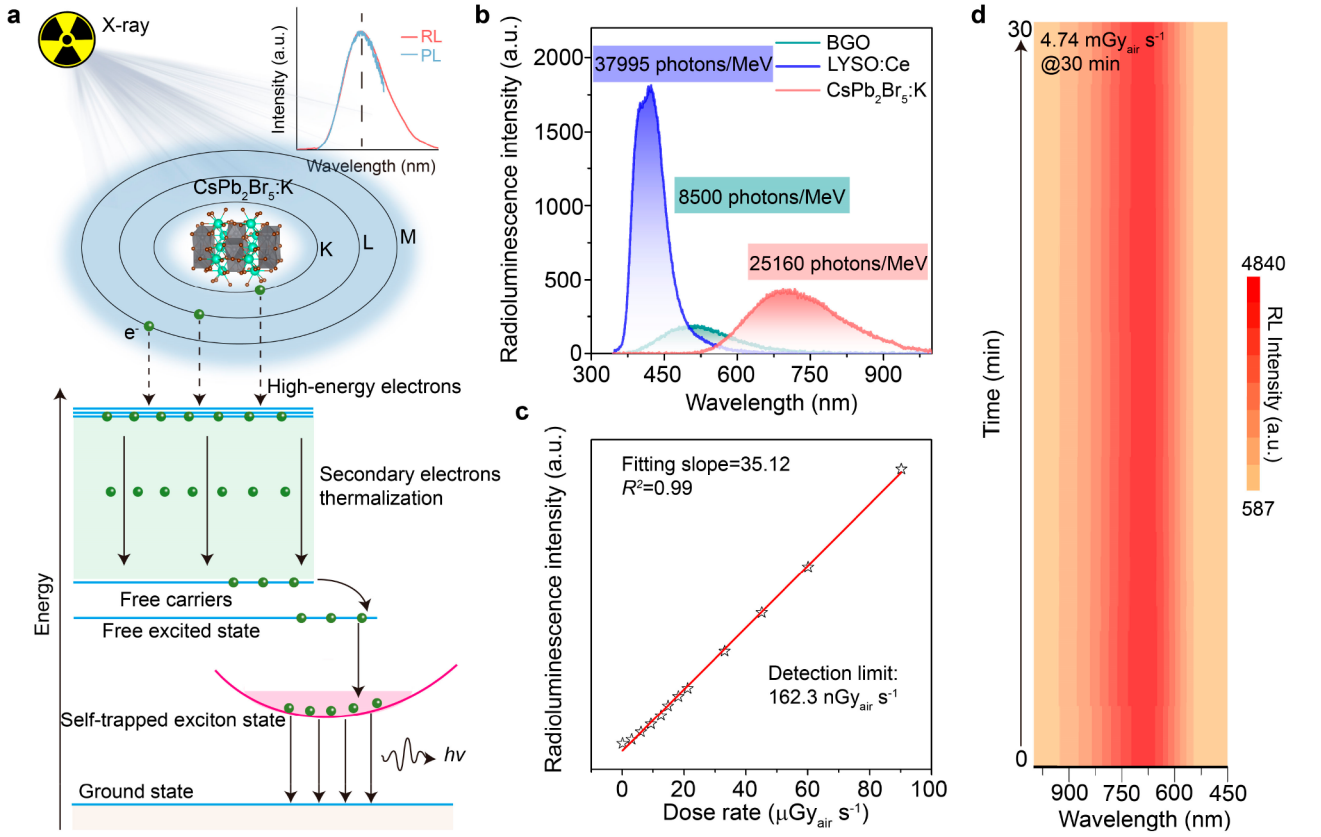

Figure 4. Scintillation performance of $CsPb_2Br_5$:K scintillators. **a**, Schematic of the scintillation mechanism in $CsPb_2Br_5$:K. **b**, Radioluminescence spectra at 40 kV using a tungsten target for measuring the relative light output of $CsPb_2Br_5$:K and LYSO:Ce wafers, with a BGO wafer as reference. All of these wafers have a thickness of 1 mm and a diameter of 7 mm. **c**, Detection limit of $CsPb_2Br_5$:K scintillator. **d**, Radioluminescence stability of $CsPb_2Br_5$:K scintillators under an X-ray dose rate of 4.74 mGy_{air} s^{-1} for 30 min (temperature, ~25 °C; humidity, ~80%).

lower energy due to the transient lattice distortion at excited states, forming self-trapped excitons followed by radioluminescence (Supplementary Figure 7b).

The scintillation performance is greatly influenced by the efficiency of X-ray absorption and emission. Hence, due to its unique combination of non-self-absorption and robust X-ray attenuation, the $CsPb_2Br_5$:K scintillator achieves a relative light output (25,160 photons per MeV) approximately 3 times greater than that of the commercial bismuth germanate (BGO) scintillator, which produces 8500 photons per MeV (Figure 4b). Additionally, its light yield is comparable to the well-studied $CsPbBr_3$ nanoscintillator and other scintillators with large Stokes shifts (Supplementary Table 3).[39] Apart from light yield, another important parameter for evaluating X-ray scintillator performance is the detection limit, defined as the X-ray dose rate at which the signal-to-noise ratio (SNR) reaches 3.[40] The calculated detection limit for $CsPb_2Br_5$:K is 162.3 nGy_{air} s^{-1} (Figure 4c and Supplementary Figure 13), significantly lower than the dose rate of 5.5 μGy_{air} s^{-1} used in X-ray diagnostics.[41] Similarly, scintillators made from $CsPb_2Br_5$ doped with Rb^+ and those with an excess of Cs^+ exhibit performance levels that are comparable to the $CsPb_2Br_5$:K scintillator (Supplementary Figures 14−16).

We next examined the material stability of $CsPb_2Br_5$:K. This material maintained strong photoluminescence for approximately 40 days and radioluminescence for 10 days, showing no structural damage even after being submerged in common solvents such as toluene, dichloromethane, water, and ethanol (Supplementary Figures 17 and 18). This enhanced stability primarily results from its low-dimensional layered crystal structure. Moreover, radioluminescence stability was assessed by exposing $CsPb_2Br_5$:K to X-rays at a dose rate of 4.74 mGy_{air} s^{-1} for 30 min under conditions of 25 °C and about 80% humidity (Figure 4d and Supplementary Figure 19). This exposure resulted in a negligible reduction in the radioluminescence intensity. To further confirm its resistance to high levels of irradiation, $CsPb_2Br_5$:K scintillators were subjected to a higher X-ray dose rate of 21,560 mGy_{air} min^{-1} for 40 min (Supplementary Figure 20). Even after enduring a total dose of 862.4 Gy_{air}, the radioluminescence intensity of $CsPb_2Br_5$:K scintillators remained at ~80% of its original intensity.

We further demonstrated the use of the $CsPb_2Br_5$:K scintillator for X-ray imaging. X-ray imaging with high contrast and fine spatial resolution is crucial to revolutionize medical diagnostics, nondestructive testing, and security screening.[42−44] The high contrast and fine resolution are highly dependent on the penetrability of radioluminescence along the scintillation screen, which is mainly limited by radioluminescence intensity and self-absorption. Benefiting from the high radioluminescence intensity and non-self-absorption, $CsPb_2Br_5$ scintillators hold great promise for high-quality X-ray imaging compared with $CsPbBr_3$ microcrystal scintillators with severe self-absorption (Supplementary Figure 21). Thus, the $CsPb_2Br_5$ powders were used to mix with polydimethylsiloxane to create a uniform scintillation film (~150 μm thick). This

https://doi.org/10.1021/acs.nanolett.3c04455
Nano Lett. XXXX, XXX, XXX−XXX

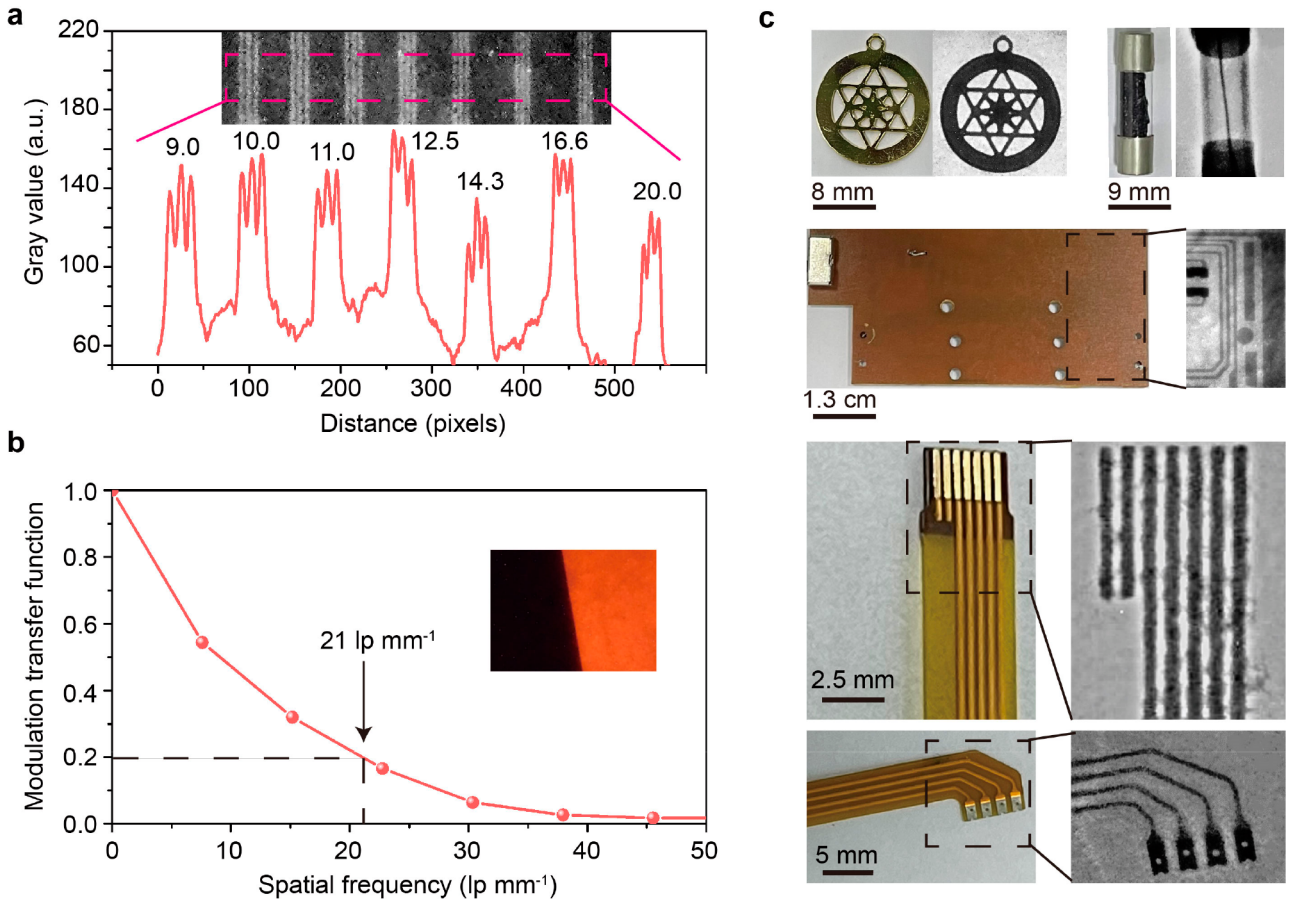

Figure 5. X-ray imaging utilizing $CsPb_2Br_5$:K scintillators. **a**, X-ray imaging of a standard X-ray resolution pattern plate, with the resulting grayscale representation ranging from 9 to 20 line pairs per millimeter (lp mm^{-1}). **b**, Modulation transfer function (MTF) of X-ray imaging obtained using the $CsPb_2Br_5$:K scintillation film. The inset is a photograph used to evaluate the MTF. **c**, X-ray imaging of a metallic accessory, a resistance wire, and integrated circuits using $CsPb_2Br_5$:K scintillators.

film enabled the X-ray imaging of the metallic accessory, resistance wire, and integrated circuits at the millimeter or micrometer scale using a homemade X-ray imaging setup, with a spatial resolution of 21 lp mm^{-1} (Figure 5a–c).

In summary, we demonstrated that it is possible to activate $CsPb_2Br_5$ materials for STE emission while effectively eliminating self-absorption. This achievement stems from a targeted approach involving ion-doping-induced lattice softening, leading to strong electron–phonon coupling. These excitons, trapped by transient lattice distortion, resemble nanoscale emitting centers within crystals, distinguishing them from the macroscopic, collective band-edge emission typical of the crystals as a whole. Notably, $CsPb_2Br_5$-based scintillators offer a compelling set of advantages, including non-self-absorption, potent X-ray stopping power, and enhanced stability. These qualities result in a high light yield and a low detection limit of 162.3 nGy_{air} s^{-1}. Moreover, we have demonstrated the capability of $CsPb_2Br_5$:K scintillation films in achieving high-resolution X-ray imaging, achieving a spatial resolution of 21 lp mm^{-1}. This achievement opens up possibilities for imaging intricate electronics. The doping approach employed in this study holds promise for diverse X-ray scintillators, including Cl-based systems with high electron–phonon coupling,[45] with implications in fields spanning medical diagnostics, materials science, security, and beyond.

■ ASSOCIATED CONTENT

Data Availability Statement

All relevant data that support the findings of this work are available from the corresponding author upon reasonable request.

Supporting Information

The Supporting Information is available free of charge at https://pubs.acs.org/doi/10.1021/acs.nanolett.3c04455.

Methods; Supplementary Figures 1–22, including optical photos, XRD results, SEM and EDS mapping, DFT calculation, carrier lifetime and PLQY, photoluminescence (PL) and temperature/power-dependent PL results, excitation spectrum, RL results, a photo of X-ray imaging, as well as attenuation efficiency; Supplementary Tables 1–3, about quantitative analysis of elements of EDS and ICP-OES as well as comparison between different scintillators; and references (PDF)

■ AUTHOR INFORMATION

Corresponding Authors

Guichuan Xing – *Joint Key Laboratory of the Ministry of Education, Institute of Applied Physics and Materials Engineering, University of Macau, Taipa, Macau 999078, P. R. China;* orcid.org/0000-0003-2769-8659; Email: gcxing@um.edu.mo

https://doi.org/10.1021/acs.nanolett.3c04455
Nano Lett. XXXX, XXX, XXX–XXX

Xian Qin − *Strait Institute of Flexible Electronics (SIFE, Future Technologies), Fujian Normal University and Strait Laboratory of Flexible Electronics (SLoFE), Fuzhou 350117, P. R. China*; Email: ifexqin@fjnu.edu.cn

Xiaogang Liu − *Department of Chemistry, National University of Singapore, Singapore 117543, Singapore; Joint School of National University of Singapore and Tianjin University, International Campus of Tianjin University, Fuzhou 350207, P. R. China; Institute of Materials Research and Engineering, Agency for Science, Technology and Research, Singapore 138634, Singapore;* orcid.org/0000-0003-2517-5790; Email: chmlx@nus.edu.sg

Authors

Jian Qiu − *Department of Chemistry, National University of Singapore, Singapore 117543, Singapore; Joint School of National University of Singapore and Tianjin University, International Campus of Tianjin University, Fuzhou 350207, P. R. China*

He Zhao − *Department of Chemistry, National University of Singapore, Singapore 117543, Singapore; Joint School of National University of Singapore and Tianjin University, International Campus of Tianjin University, Fuzhou 350207, P. R. China*

Zhen Mu − *Department of Chemistry, National University of Singapore, Singapore 117543, Singapore*

Jiaye Chen − *Department of Chemistry, National University of Singapore, Singapore 117543, Singapore*

Hao Gu − *Joint Key Laboratory of the Ministry of Education, Institute of Applied Physics and Materials Engineering, University of Macau, Taipa, Macau 999078, P. R. China*

Chang Gu − *Department of Chemistry, National University of Singapore, Singapore 117543, Singapore; Joint School of National University of Singapore and Tianjin University, International Campus of Tianjin University, Fuzhou 350207, P. R. China*

Complete contact information is available at: https://pubs.acs.org/10.1021/acs.nanolett.3c04455

Author Contributions

J.Q. and X.L. conceived and designed the experiments. X.L. supervised the project. J.Q. prepared the materials and conducted the experiments and characterizations. Z.M., H.G., and G.X. helped perform the optical characterization. J.C. helped conduct the high-resolution TEM. X.Q. helped conduct the DFT calculation analysis. H.Z. helped conduct the X-ray measurements. J.Q., C.G., X.Q., and X.L. wrote the manuscript with input from all authors.

Funding

This research was primarily funded through National Research Foundation and the Prime Minister's Office of Singapore under its Competitive Research Program (CRP Award No. NRF-CRP23-2019-0002) and NRF Investigatorship Programme (Award No. NRF-NRFI05-2019-0003). G.X. acknowledges the Science and Technology Development Fund, Macao SAR (File no. 0082/2021/A2, 006/2022/ALC), UM's research fund (File no. MYRG2022-00241-IAPME, MYRG-CRG2022-00009-FHS), and the Natural Science Foundation of China (61935017, 62175268).

Notes

The authors declare no competing financial interest.

REFERENCES

(1) Büchele, P.; Richter, M.; Tedde, S. F.; Matt, G. J.; Ankah, G. N.; Fischer, R.; Biele, M.; Metzger, W.; Lilliu, S.; Bikondoa, O.; Macdonald, J. E.; Brabec, C. J.; Kraus, T.; Lemmer, U.; Schmidt, O. X-ray Imaging with Scintillator-Sensitized Hybrid Organic Photodetectors. *Nat. Photonics* **2015**, *9*, 843−848.

(2) Wei, W.; Zhang, Y.; Xu, Q.; Wei, H.; Fang, Y.; Wang, Q.; Deng, Y.; Li, T.; Gruverman, A.; Cao, L.; Huang, J. Monolithic Integration of Hybrid Perovskite Single Crystals with Heterogenous Substrate for Highly Sensitive X-ray Imaging. *Nat. Photonics* **2017**, *11*, 315−321.

(3) Yi, L.; Hou, B.; Zhao, H.; Liu, X. X-ray-to-Visible Light-Field Detection Through Pixelated Colour Conversion. *Nature* **2023**, *618*, 281−286.

(4) Sakhatskyi, K.; Turedi, B.; Matt, G. J.; Wu, E.; Sakhatska, A.; Bartosh, V.; Lintangpradipto, M. N.; Naphade, R.; Shorubalko, I.; Mohammed, O. F.; Yakunin, S.; Bakr, O. M.; Kovalenko, M. V. Stable Perovskite Single-Crystal X-ray Imaging Detectors with Single-Photon Sensitivity. *Nat. Photonics* **2023**, *17*, 510−517.

(5) Tsai, H.; Shrestha, S.; Pan, L.; Huang, H.-H.; Strzalka, J.; Williams, D.; Wang, L.; Cao, R. L.; Nie, W.-Y. Quasi-2D Perovskite Crystalline Layers for Printable Direct Conversion X-Ray Imaging. *Adv. Mater.* **2022**, *34*, No. 2106498.

(6) Pei, P.; Chen, Y.; Sun, C.; Fan, Y.; Yang, Y.; Liu, X.; Lu, L.; Zhao, M.; Zhang, H.; Zhao, D.; Liu, X.; Zhang, F. X-ray-Activated Persistent Luminescence Nanomaterials for NIR-II Imaging. *Nat. Nanotechnol.* **2021**, *16*, 1011−1018.

(7) Chu, D.; Jia, B.; Liu, N.; Zhang, Y.; Li, X.; Feng, J.; Pi, J.; Yang, Z.; Zhao, G.; Liu, Y.; Liu, S. F.; Park, N.-G. Lattice Engineering for Stabilized Black $FAPbI_3$ Perovskite Single Crystals for High-Resolution X-ray Imaging at the Lowest Dose. *Sci. Adv.* **2023**, *9*, No. eadh2255.

(8) Jiang, J.; Xiong, M.; Fan, K.; Bao, C.; Xin, D.; Pan, Z.; Fei, L.; Huang, H.; Zhou, L.; Yao, K.; Zheng, X.; Shen, L.; Gao, F. Synergistic Strain Engineering of Perovskite Single Crystals for Highly Stable and Sensitive X-ray Detectors with Low-Bias Imaging and Monitoring. *Nat. Photonics* **2022**, *16*, 575−581.

(9) Yang, Y.-M.; Li, Z.-Y.; Zhang, J.-Y.; Lu, Y.; Guo, S.-Q.; Zhao, Q.; Wang, X.; Yong, Z.-J.; Li, H.; Ma, J.-P.; Kuroiwa, Y.; Moriyoshi, C.; Hu, L.-L.; Zhang, L.-Y.; Zheng, L.-R.; Sun, H.-T. X-ray-Activated Long Persistent Phosphors Featuring Strong UVC Afterglow Emissions. *Light Sci. Appl.* **2018**, *7*, 88.

(10) He, Y.; Petryk, M.; Liu, Z.; Chica, D. G.; Hadar, I.; Leak, C.; Ke, W.; Spanopoulos, I.; Lin, W.; Chung, D. Y.; Wessels, B. W.; He, Z.; Kanatzidis, M. G. $CsPbBr_3$ Perovskite Detectors with 1.4% Energy Resolution for High-Energy γ-rays. *Nat. Photonics* **2021**, *15*, 36−42.

(11) Michail, C.; Koukou, V.; Martini, N.; Saatsakis, G.; Kalyvas, N.; Bakas, A.; Kandarakis, I.; Fountos, G.; Panayiotakis, G.; Valais, I. Luminescence Efficiency of Cadmium Tungstate ($CdWO_4$) Single Crystal for Medical Imaging Applications. *Crystals* **2020**, *10*, 429.

(12) Markotter, H.; Muller, B. R.; Kupsch, A.; Evsevleev, S.; Arlt, T.; Ulbricht, A.; Dayani, S.; Bruno, G. A Review of X-Ray Imaging at the BAMline (BESSY II). *Adv. Eng. Mater.* **2023**, *25*, No. 2201034.

(13) Nagarkar, V. V.; Gupta, T. K.; Miller, S. R.; Klugerman, Y.; Squillante, M. R.; Entine, G. Structured CsI(Tl) Scintillators for X-ray Imaging Applications. *IEEE Trans. Nucl. Sci.* **1998**, *45*, 492−496.

(14) Cao, F.; Yu, D.; Ma, W.; Xu, X.; Cai, B.; Yang, Y. M.; Liu, S.; He, L.; Ke, Y.; Lan, S.; Choy, K.-L.; Zeng, H.-B. Shining Emitter in a Stable Host: Design of Halide Perovskite Scintillators for X-ray Imaging from Commercial Concept. *ACS Nano* **2020**, *14*, 5183−5193.

(15) Zhang, M.; Zhu, J.; Yang, B.; Niu, G.; Wu, H.; Zhao, X.; Yin, L.; Jin, T.; Liang, X.; Tang, J. Oriented-Structured $CsCu_2I_3$ Film by Close-Space Sublimation and Nanoscale Seed Screening for High-Resolution X-ray Imaging. *Nano Lett.* **2021**, *21*, 1392−1399.

(16) Chen, Q.; Wu, J.; Ou, X.; Huang, B.; Almutlaq, J.; Zhumekenov, A. A.; Guan, X.; Han, S.; Liang, L.; Yi, Z.; Li, J.; Xie, X.; Wang, Y.; Li, Y.; Fan, D.; Teh, D. B. L.; All, A. H.; Mohammed, O. F.; Bakr, O. M.; Wu, T.; Bettinelli, M.; Yang, H.; Huang, W.; Liu, X.

All-Inorganic Perovskite Nanocrystal Scintillators. *Nature* **2018**, *561*, 88−93.
(17) Zhang, H.; Yang, Z.; Zhou, M.; Zhao, L.; Jiang, T.; Yang, H.; Yu, X.; Qiu, J.; Yang, Y. M.; Xu, X. Reproducible X-ray Imaging with a Perovskite Nanocrystal Scintillator Embedded in a Transparent Amorphous Network Structure. *Adv. Mater.* **2021**, *33*, No. 2102529.
(18) Wang, J.-X.; Gutierrez-Arzaluz, L.; Wang, X.-J.; He, T.-Y.; Zhang, Y.-H.; Eddaoudi, M.; Bakr, O. M.; Mohammed, O. F. Heavy-Atom Engineering of Thermally Activated Delayed Fluorophores for High-Performance X-ray Imaging Scintillators. *Nat. Photonics* **2022**, *16*, 869−875.
(19) Ma, W.-B.; Su, Y.-R.; Zheng, Q.-S.; Deng, C.; Pasquali, L.; Zhu, W.-J.; Tian, Y.; Ran, P.; Chen, Z.; Yang, G.-Y.; Liang, G.-J.; Liu, T.-Y.; Zhu, H.-M.; Huang, P.; Zhong, H.-Z.; Wang, K.-W.; Peng, S.-Q.; Xia, J.-L.; Liu, H.-F.; Liu, X.; Yang, Y. M. Thermally Activated Delayed Fluorescence (TADF) Organic Molecules for Efficient X-ray Scintillation and Imaging. *Nat. Mater.* **2022**, *21*, 210−216.
(20) Gan, N.; Zou, X.; Dong, M.-Y.; Wang, Y.-Z.; Wang, X.; Lv, A.-Q.; Song, Z.-C.; Zhang, Y.-Y.; Gong, W.-Q.; Zhao, Z.; Wang, Z.-Y.; Zhou, Z.-X.; Ma, H.-L.; Liu, X.-W.; Chen, Q.-S.; Shi, H.-F.; Yang, H.-H.; Gu, L.; An, Z.-F.; Huang, W. Organic Phosphorescent Scintillation From Copolymers By X-ray Irradiation. *Nat. Commun.* **2022**, *13*, 3995.
(21) Xu, L.-J.; Lin, X.-S.; He, Q.-Q.; Worku, M.; Ma, B.-W. Highly Efficient Eco-friendly X-ray Scintillators Based on An Organic Manganese Halide. *Nat. Commun.* **2020**, *11*, 4329.
(22) Zhang, N.; Ou, L.; Dai, S.-H.; Xie, G.-H.; Han, C.-M.; Zhang, J.; Huo, R.; Hu, H.; Chen, Q.-S.; Huang, W.; Xu, H. Intramolecular Charge Transfer Enables Highly-Efficient X-ray Luminescence in Cluster Scintillators. *Nat. Commun.* **2023**, *14*, 2901.
(23) Zhang, X.; Qiu, H.; Luo, W.; Huang, K.; Chen, Y.; Zhang, J.; Wang, B.; Peng, D.; Wang, Y.; Zheng, K. High-Performance X-Ray Imaging using Lanthanide Metal-Organic Frameworks. *Adv. Sci.* **2023**, *10*, No. 2207004.
(24) Brennan, M. C.; Herr, J. E.; Nguyen-Beck, T. S.; Zinna, J.; Draguta, S.; Rouvimov, S.; Parkhill, J.; Kuno, M. Origin of the Size-Dependent Stokes Shift in $CsPbBr_3$ Perovskite Nanocrystals. *J. Am. Chem. Soc.* **2017**, *139*, 12201−12208.
(25) He, H.; Mei, S.; Chen, Z.; Liu, S.; Wen, Z.; Cui, Z.; Yang, D.; Zhang, W.; Xie, F.; Yang, B.; Guo, R.; Xing, G. Thioacetamide-Ligand-Mediated Synthesis of $CsPbBr_3$-$CsPbBr_3$ Homostructured Nanocrystals with Enhanced Stability. *J. Mater. Chem. C* **2021**, *9*, 11349−11357.
(26) Wang, Y.; Li, M.; Chai, Z.; Wang, Y.; Wang, S. Perovskite Scintillators for Improved X-ray Detection and Imaging. *Angew. Chem., Int. Ed.* **2023**, *62*, No. e202304638.
(27) Wang, X.; Niu, G.-W.; Zhou, Z.-X.; Song, Z.-C.; Qin, K.; Yao, X.-K.; Yang, Z.-J.; Wang, X.-Z.; Wang, H.; Liu, Z.; Yin, C.-Z.; Ma, H.-L.; Shen, K.; Shi, H.-F.; Yin, J.; Chen, Q.-S.; An, Z.-F.; Huang, W. Halogenated Thermally Activated Delayed Fluorescence Materials for Efficient Scintillation. *Research* **2023**, *6*, 0090.
(28) Yu, Y.; Xiang, L.; Zhang, X.; Zhang, L.; Ni, Z.; Zhu, Z.; Liu, Y.; Lan, J.; Liu, W.; Xie, G.; Feng, G.; Tang, B.-Z. Pure Organic AIE Nanoscintillator for X-ray Mediated Type I and Type II Photodynamic Therapy. *Adv. Sci.* **2023**, *10*, No. 2302395.
(29) Dursun, I.; Bastiani, M. D.; Turedi, B.; Alamer, B.; Shkurenko, A.; Yin, J.; EI-Zohry, A. M.; Gereige, I.; Alsaggaf, A.; Mohammed, O. F.; Eddaoudi, M.; Bakr, O. M. $CsPb_2Br_5$ Single Crystals: Synthesis and Characterization. *ChemSusChem* **2017**, *10*, 3746−3749.
(30) Liu, Z.; Qin, X.; Chen, Q.-H.; Jiang, T.; Chen, Q.; Liu, X. Metal−Halide Perovskite Nanocrystal Superlattice: Self-Assembly and Optical Fingerprints. *Adv. Mater.* **2023**, *35*, No. 2209279.
(31) Cheng, S.-J.; Chen, Y.; Zhong, H.-Z. Centimeter-Sized Na-Doped $CsPb_2Br_5$ Single Crystals with Efficient Self-Trapped Exciton Emission. *Cryst. Growth Des.* **2022**, *22*, 4025−4030.
(32) Hu, H.; Liu, Y.; Xie, Z.; Xiao, Z.; Niu, G.; Tang, J. Observation of Defect Luminescence in 2D Dion-Jacobson Perovskites. *Adv. Optical Mater.* **2021**, *9*, No. 2101423.
(33) Luo, J.-J.; Wang, X.-M.; Li, S.-R.; Liu, J.; Guo, Y.-M.; Niu, G.-D.; Yao, L.; Fu, Y.-H.; Gao, L.; Dong, Q.-S.; Zhao, C.-Y.; Leng, M.-Y.; Ma, F.-S.; Liang, W.-X.; Wang, L.-D.; Jin, S.-Y.; Han, J.-B.; Zhang, L.-J.; Etheridge, J.; Wang, J.-B.; Yan, Y.-F.; Sargent, E. H.; Tang, J. Efficient and Stable Emission of Warm-White Light From Lead-Free Halide Double Perovskites. *Nature* **2018**, *563*, 541−545.
(34) Li, X.; Lian, X.; Pang, J.; Luo, B.; Xiao, Y.; Li, M.-D.; Huang, X.-C.; Zhang, J. Z. Defect-Related Broadband Emission in Two-Dimensional Lead Bromide Perovskite Microsheets. *J. Phys. Chem. Lett.* **2020**, *11*, 8157−8163.
(35) Chen, H.; Pina, J. M.; Yuan, F.; Johnston, A.; Ma, D.; Chen, B.; Li, Z.; Dumont, A.; Li, X.; Liu, Y.; Hoogland, S.; Zajacz, Z.; Lu, Z.; Sargent, E. H. Multiple Self-Trapped Emissions in the Lead-Free Halide $Cs_3Cu_2I_5$. *J. Phys. Chem. Lett.* **2020**, *11*, 4326−4330.
(36) Wang, Y.-Z.; Zhao, W.-J.; Guo, Y.-Y.; Hu, W.-B.; Peng, C.-X.; Li, L.; Wei, Y.; Wu, Z.-B.; Xu, W.-D.; Li, X.-Y.; Suh, Y. D.; Liu, X.-W.; Huang, W. Efficient X-ray Luminescence Imaging with Ultrastable and Eco-friendly Copper(I)-Iodide Cluster Microcubes. *Light Sci. Appl.* **2023**, *12*, 155.
(37) Hadjiev, V. G.; Wang, C.; Wang, Y.; Su, X.; Calderon, H. A.; Hernandez, F. R.; Wang, Z.-M.; Bao, J.-M. Phonon Fingerprints of $CsPb_2Br_5$. *J. Phys.: Condens. Matter* **2018**, *30*, No. 405703.
(38) Yang, H.; Chen, X.; Lu, H.; Li, Y.; Sun, W.; Zhang, Y.; Liu, X.; Long, G.; Zhang, L.; Li, X. Self-Trapped Excitons-Based Warm-White Afterglow by Room-Temperature Engineering toward Intelligent Multi-Channel Information System. *Adv. Funct. Mater.* **2023**, No. 2311437.
(39) Maddalena, F.; Xie, A.-Z.; Chi, X. Y.; Begum, R.; Witkowski, M. E.; Makowski, M.; Mahler, B.; Drozdowski, W.; Springham, S. V.; Rawat, R. S.; Mathews, N.; Dujardin, C.; Birowosuto, M. D.; Dang, C. Deterministic Light Yield, Fast Scintillation, and Microcolumn Structures in Lead Halide Perovskite Nanocrystals. *J. Phys. Chem. C* **2021**, *125*, 14082−14088.
(40) Zhang, H.; Yang, Z.; Zhou, M.; Zhao, L.; Jiang, T.-M.; Yang, H.-Y.; Yu, X.; Qiu, J.-B.; Yang, Y. M.; Xu, X.-H. Reproducible X-ray Imaging with A Perovskite Nanocrystal Scintillator Embedded in A Transparent Amorphous Network Structure. *Adv. Mater.* **2021**, *33*, No. 2102529.
(41) Shearer, D. R.; Bopaiah, M. Dose Rate Limitations of Integrating Survey Meters for Diagnostic X-ray Surveys. *Health Phys.* **2000**, *79*, S20−1.
(42) Zhang, C.-Y.; Yao, S.-K.; Xu, C.; Chang, Y.-N.; Zong, Y.-B.; Zhang, K.; Zhang, X.-Z.; Zhang, L.-J.; Chen, C.-Y.; Zhao, Y.-L.; Jiang, H.-D.; Gao, X.-Y.; Wang, Y.-L. 3D Imaging and Quantification of the Integrin at a Single-Cell Base on a Multisignal Nanoprobe and Synchrotron Radiation Soft X-ray Tomography Microscopy. *Anal. Chem.* **2021**, *93*, 1237−1241.
(43) Ghosh, J.; O'Neill, J.; Masteghin, M. G.; Braddock, I.; Crean, C.; Dorey, R.; Salway, H.; Anaya, M.; Reiss, J.; Wolfe, D.; Sellin, P. Surfactant-Dependent Bulk Scale Mechanochemical Synthesis of $CsPbBr_3$ Nanocrystals for Plastic Scintillator-Based X-ray Imaging. *ACS Appl. Nano Mater.* **2023**, *6*, 14980−14990.
(44) He, T.-Y.; Zhou, Y.; Yuan, P.; Yin, J.; Gutierrez-Arzaluz, L.; Chen, S.-L.; Wang, J.-X.; Thomas, S.; Alshareef, H. N.; Bakr, O. M.; Mohammed, O. F. Copper Iodide Inks for High-Resolution X-ray Imaging Screens. *ACS Energy Lett.* **2023**, *8*, 1362−1370.
(45) Han, Y.; Yin, J.; Cao, G.; Yin, Z.; Dong, Y.; Chen, R.; Zhang, Y.; Li, N.; Jin, S.; Mohammed, O. F.; Cui, B.-B.; Chen, Q. Exciton Self-Trapping for White Emission in 100-Oriented Two-Dimensional Perovskites via Halogen Substitution. *ACS Energy Lett.* **2022**, *7*, 453−460.

https://doi.org/10.1021/acs.nanolett.3c04455
Nano Lett. XXXX, XXX, XXX−XXX